JOTCS A
Journal of the Turkish Chemical Society
Section: A
Chemistry
TURKISH CHEMICAL SOCIETY

Adsorptive Elimination of Methyl Orange Dye over the Activated Carbon Derived from Bitter Almond Shells: An Isothermal, Thermodynamic, and Kinetic Study

Rana H. Al-Hyali[1], Wael A. Alqazzaz[1], Duaa H. Altamer[2,*]

[1]Department of Chemistry, College of Science, Mosul University, Mosul, Iraq
[2]Department of New and Renewable Energies, College of Science, Mosul University, Mosul, Iraq

Abstract: Bitter almond shells (BAS) were inspected as a cheap source for the creation of activated carbon (AC) through the optimized $ZnCl_2$-activation approach. The raw BAS were impregnated with $ZnCl_2$ at multiple ratios (1:1 - 3:1 $ZnCl_2$:BAS), followed by carbonization at various temperatures (400 – 800 °C) for different durations (30 – 120 minutes) in a tubular reactor. The typical AC sample was produced with a yield of 23.46% using a 1:1 $ZnCl_2$:BAS impregnation ratio at 500 °C for 60 minutes. The ideal AC sample was identified by BET surface area (SA_{BET}), Boehm titration method, point of zero charges (pH_{PZC}), FESEM, XRD, FTIR, and EDX. The identification consequences revealed that this sample is mesoporous with SA_{BET}, iodine number, total pore volume, and average pore width of 1221.60 m^2/g, 1444.23 mg/g,1.50 cm^3/g, and 4.98 nm, respectively. The adsorptive removal (AR) of methyl orange (MO) dye from its aqueous phase by this AC was accomplished at various solution pH (2–10), diverse mass of the AC (0.05-0.4 g), multiple initial concentrations (50–400 mg/L), variable temperature (30-50 °C) and diverse contact periods (0–420 min) in a batch- mode operation. The maximum monolayer adsorption capacity of 224.71 mg/g was obtained at 323 K, pH= 2.0, 400 mg/L initial concentration of MO, 0.25 g AC dose, and 420 minutes contact period. The kinetic outcomes best fitted to the pseudo-2^{nd} -order kinetics model, while the MO equilibrium capacity obeyed the Langmuir model rather than other models. Thermodynamic studies of the MO adsorption by the BAS-derived AC disclosed that the adsorption was spontaneous and endothermic. The adsorption mechanism of MO by the declared AC primarily involved electrostatic attractions and hydrogen bonding interaction. This work demonstrates that BAS is an excellent raw material for producing low-cost and effectual mesoporous AC carbon with substantive surface area.

Keywords: Activated carbon; Bitter almond shells; Adsorption isotherms and kinetics ; Methyl Orange Dye.

Submitted: November 10, 2022. **Accepted:** January 30, 2023.

Cite this: Al-Hyali RH, Alqazzaz WA, Altamer DH. Adsorptive Elimination of Methyl Orange Dye over the Activated Carbon Derived from Bitter Almond Shells: An Isothermal, Thermodynamic, and Kinetic Study. JOTCSA. 2023;10(2):339–58.

DOI: https://doi.org/10.18596/jotcsa.1177543.

***Corresponding author. E-mail:** duaaaaltamer@uomosul.edu.iq.

1. INTRODUCTION

The production of colored and fashioned clothes is based on utilizing organic dyes (ODs) (1). Multiple industries, including dyeing, textile, food processing, printing, papermaking, and electroplating, are based on the utilization of ODs (2). Nonetheless, ejecting the leftover dyes as per textile discharges as a wastewater causes a huge environmental hazard to both the surface and underground water sources (3). Also, because of their slow biodegradability, the occurrence of ODs in wastewater will affect human health (4). Several effective and profitable procedures have been followed to treat wastewater ejected by the textile industry (5). Membrane separation (6), oxidation (3), precipitation (7), ion-exchange (8), coagulation (9), flocculation (10), and adsorption

(11-13) are the most traditional routes utilized to solve problems associated with ODs effluents. Nevertheless, adsorption is the most efficient approach for ODs removal because it is cheap, eco-friendly, and possesses high elimination ability (14).

Numerous effective adsorbents, including biowastes (15), modified biowastes (16), zeolites (17), fly ash (18), biochar (19), polymeric materials (20), modified biochar (21), AC (22), and AC composites (23) were utilized in the adsorptive elimination of diverse ODs from their aqueous medium. Amongst the most effective adsorbents that have employed in the adsorptive removal (AR) of ODs from polluted wasters is AC. This adsorbent owns an elevated surface area, in the range of 500 m^2/g and 2000 m^2/g, besides its low-density, high adsorptive capacity, high chemical stability, and high porosity. Also, one of the most attractive features of the AC is its surface, which contains numerous functional groups, particularly oxygen groups (24, 25). The primary feedstocks employed in AC production at the commercial scale are wood, coal, and lignite. These raw materials are relatively expensive, which raises the production cost of AC, besides making the utilization of AC in controlling water pollution unwelcomed (25). The selection of low-cost feedstocks for creating AC has become an important issue. In this regard, agricultural wastes have been proposed as a significant feedstock for AC production due to their renewability and low cost. Consequently, recent investigations focused on AC production from such cheap organic-wastes (26).

Methyl orange (MO) is a carcinogenic dye that belongs to the azo class of dyes. It is an anionic dye and a chemically water-stable dye. Thus, its removal from wastewater via conventional routes of purification is hard. Its presence in water affects the aquatic plants' response to photosynthesis, as it lessens the ability of light to penetrate water (27). Adsorption was widely implemented in the adsorptive elimination of MO from wastewater. Multiple bio-wastes were employed in AC preparation to eliminate MO dye from its aqueous medium. As reported by Abdullah et al., the corn con-derived AC was utilized in the adsorptive elimination of MO dye (27). Pomelo peel wastes derived biochar was activated with H_3PO_4 and then applied to eliminate MO from wastewater (28). The AR of MO dye from wastewater was conducted using the Mahagoni Bark-derived AC established by Chakraborty et al. (29). Sea mango-derived AC was prepared via the H_3PO_4 activation method and activated using microwave radiation to be implemented in MO removal from its aqueous solution (30). However, to the authors' knowledge, the creation of AC using bitter almond shells (BAS) as a precursor by the $ZnCl_2$-activation method, with exploring the impact of the preparation conditions on the yield and iodine number (IN) of the created AC has not been established yet. Moreover, employing the typical AC sample in the AR of MO dye from its aqueous phase has not been reported yet, which encouraged us to conduct this work.

This study focuses on using BAS as a raw material to create AC using the $ZnCl_2$ activation approach through optimizing the impact of the impregnation ratio (IR) of $ZnCl_2$ besides the activation temperature and duration, on the AC yield and IN. The typical sample of the AC was further identified by numerous techniques to assess its structure and adsorptive capacity. Factors affecting the adsorption of MO by the as-prepared AC were optimized as well. The AC's adsorption kinetics, isotherms, and thermodynamics of MO elimination were also inspected.

2. EXPERIMENTAL

2.1 Chemicals and Feedstock

Fresh bitter almond fruit was purchased from markets situated in Dohuk Governorate, north of Iraq. Preparation and analysis of the prepared AC needed multiple chemicals, such as iodine solution (0.05 mol/L (0.1 N)), $ZnCl_2$ (98.0 – 100.5 %), HCl (36.5 – 38.0 %), $Na_2S_2O_3.5H_2O$ (99.0 – 100.5 %), and NaOH, pellets (98.50 %) were acquired from Scharlab (Scharlab, Barcelona, Spain). They were employed as received. The MO dye, which possesses an MW of 327.33 g/mol and a chemical formula of $C_{14}H_{14}N_3NaO_3S$, was provided by Merck. Figure 1 shows the chemical structure of Eriochrome Black T (Erio-T) dye.

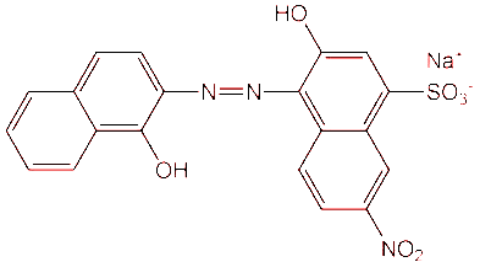

Figure 1: Chemical structure of Erio-T dye.

2.2 Analysis of BAS

Shells were stripped from the bitter almond fruit and used as a feed in AC synthesis. The BAS was rinsed with tap water, followed by DW to remove dust and foreign impurities. After heating to dryness in an oven at 110 °C for a day so as to guarantee the entire removal of washing water. To pulverize the dry BAS, an industrial electrical grinder was employed. The obtained powder was sieved to produce 60 mesh-sized particles. The ultimate analysis of the dried BAS was accomplished to recognize its C, H, N, S, and O content. The ASTM 3174 and ASTM 3175 were followed to specify the proximate analysis of the BAS, namely fixed carbon humidity, volatiles, and

ash. Finally, the BAS component analysis was accomplished per the method established by Mansor et al. (31) to recognize their contents of cellulose, hemicellulose, and lignin.

2.3 Preparation of AC from BAS

The $ZnCl_2$ activation method was employed in creating the AC from the dried BAS. The dried BAS was immersed in solutions containing multiple mass ratios of $ZnCl_2$: BAS (1:1,1-2, and 3:1) and magnetically stirred for 12 h. The attained mixtures were then dried at 80 °C until dryness. Later, the dried mixtures were heated at numerous temperatures (400 °C to 700 °C) for different durations (0.5 h- 2.0 h) in a tubular furnace at a 10 °C/min heating rate. After activation, the activated samples were treated with a solution of 0.50 N HCl with stirring to eliminate the excess of $ZnCl_2$. The samples were then carefully washed with DW until a neutral pH was reached. After being oven-dried at 105 °C for 10 h, the activated samples were then maintained in a tight container (32). Calculating the yield of the AC was done as follows:

$$AC\ Yield(\%) = \frac{Weight\ of\ AC}{Weight\ of\ BAS\ used} \times 100 \quad \text{(Eq. 1)}$$

2.4 Identification of the AC

The typical AC sample was characterized by multiple techniques, including Field Emission-Scanning Electron Microscope (FESEM) on an instrument (A TESCAN MIRA FESEM, Czech Republic) attached to an energy-dispersive analysis X-ray (EDX) to determine the AC surface morphology and elemental analysis, respectively. The BET surface area (SA_{BET}) of the AC, besides its pore volume, was measured on a BELSORP MINI II, Japan, surface area and porosimetry analyzer. A Malvern Panalytical X-ray diffractometer, UK, was used to inspect the amorphous and crystal structure of the created AC. Surface functional groups containing oxygen on the AC surface were determined through the titration method (33). A Fourier transform infrared (FTIR) (JASCO V-630, USA) was utilized in identifying the surface functional groups and chemical bonds. The ASTM D4607-14 was followed in determining the iodine number (IN) of the so-created AC samples.

2.5 Adsorption Equilibrium Studies

The MO adsorption experiments by the so-synthesized AC were accomplished via a batch process. Firstly, a 500 mg/L stock solution of MO was prepared. Next, solutions of various concentrations of MO were prepared from the stock solution through dilution to prepare the standardization curve. A known weight of the AC was mixed with a given volume of MO solution at the optimized pH value, and the mixtures were shaken at room temperature (30 °C) for a specified period. After attaining the equilibrium, the mixture was separated by centrifugation at 6000 rpm for 5 minutes. The concentration of the residual dye in the solution was spectrophotometrically determined using a UV–Vis spectrophotometer at the maximum wavelength (λ_{max}=464 nm). The amount of adsorbed dye, q_e (mg/g), was calculated as per the following equations:

$$MO(\%) = \frac{(C_0 - C_e)}{C_0} \times 100 \quad \text{(Eq. 2)}$$

$$q_e = \frac{(C_o - C_e)V}{W} \quad \text{(Eq. 3)}$$

where, C_0 and C_e are the MO initial and equilibrium concentrations (mg/L), respectively, while V (L) and W (g) are the volume of MO solution employed and the AC mass utilized in the AR process.

2.6 Equilibrium Models of Adsorption Isotherms

The adsorption isotherm describes the equilibrium between the adsorbent and the adsorbate in the solution. It can be employed to express the adsorbent capacity at equilibrium by describing the distribution of the adsorbate molecules between the solution phase and the solid phase equilibrium. It is also imperative to explain the solute's interactions with adsorbents and optimize its usage (33). Three famous isotherms of adsorption, namely the Langmuir, Freundlich, and Temkin, were compared to clarify the adsorption mechanism that will describe the adsorption data at equilibrium. The Langmuir model adopts monolayer adsorption onto the adsorbent surface, and its linearized form can be expressed as follows:

$$\frac{C_e}{q_e} = \frac{1}{q_m K_L} + \frac{C_e}{q_m} \quad \text{(Eq. 4)}$$

where, q_m (mg/g) and K_L (L/mg) express the maximum quantity of the contaminant adsorbed per unit mass of adsorbent and the Langmuir constant, respectively. K_L relates to the affinity of the binding sites, and its higher value means that the adsorption of the solute by the adsorbent is easier. The Freundlich isotherm, which refers to the multilayer adsorption of solute onto the adsorbent surface, is an empirical equation. The linearized form is this isotherm can be given as follows:

$$\ln q_e = \ln K_F + \frac{1}{n} \ln C_e \quad \text{(Eq. 5)}$$

where, K_F (mg/g) and n express respectively the Freundlich adsorption capacity and intensity. According to the Temkin isotherm, whose linear equation is shown in equation (6), a decrease in

adsorption heat occurs as a function of temperature (33).

$$q_e = \frac{RT}{B} \ln KT + \frac{RT}{B} \ln C_e \qquad \text{(Eq. 6)}$$

where, R is the universal gas constant (8.314 J/(mol), K_T is the equilibrium binding constant (L/g) and B (J/mol) represents the heat of adsorption heat.

2.7 Adsorption models of kinetics

The pseudo-1st-order and pseudo-2nd-order kinetic models, whose equations are respectively provided in Eqs. (7) and (8), were used to examine the adsorption kinetics.

$$\ln\left(q_e - q_t\right) = \ln\left(q_e\right) - k.t \qquad \text{(Eq. 7)}$$

$$\frac{t}{q_t} = \frac{1}{k_2 q_e^{\,2}} + \frac{t}{q_e} \qquad \text{(Eq. 8)}$$

where, q_t (mg/g) and q_e (mg/g) are the quantity of the solute adsorbed at time t (minute) at equilibrium, while k (min^{-1}) and k_2 (g/(mg min) are respectively the pseudo-first-order and pseudo-second-order rate constants.

2.8 Intraparticle Diffusion Model

This model of diffusion is usually used to recognize the mechanism of the contaminant adsorption for design purposes. This model suggests that in most adsorption processes, the adsorption changes almost proportionally with $t^{½}$ more than with the contact time (34). This model of diffusion is represented in the following equation:

$$q_t = K_{id} t^{0.5} + C \qquad \text{(Eq. 9)}$$

where, q_t is the quantity of contaminant adsorbed at time t, while $t^{0.5}$ is the square root of the time, C is the intercept, and K_{id} (mg g^{-1} $min^{-0.5}$) is the intraparticle diffusion rate constant.

2.9 Reusability Studies

The reusability tests of the MO by the prepared AC were investigated similarly to the batch adsorption studies. The typical mass of the AC was mixed with 100 mL of MO solution. The mixture was shaken for a specified period. After filtration, the MO concentration remained after the adsorption process was measured employing a UV-Vis spectrophotometer, while the AC was treated with a solution of 0.1 M HCl for 5h. After washing until neutral water was obtained, the AC was dried at 110 °C to ensure the complete dryness of the sample and then implemented in the AR of MO for 5 cycles (34).

3. RESULTS AND DISCUSSION

3.1 Analysis of the Raw BAS

The ultimate analysis results of the raw BAS exhibited that its content of C, H, S, N, and O is 49.97%, 4.88%, 0.61%, 0.10%, and 44.44 %, respectively. The high C % for the BAS suggests its suitability as an AC precursor. The proximate analysis outcomes of the authentic BAS were moisture = 2.23%, volatile matters = 74.02 %, ash = 1.21 %, and fixed carbon = 22.54 %. The high fixed carbon % of BAS recommends its utilization in the synthesis of AC. Also, a minimum ash % precursor could create low-ash content AC (35). The component analysis of the BAS showed that it contains 4.0 % extractives, lignin = 22.12 %, hemicellulose =25.55 %, and Cellulose = 48.22 %. The lignin, cellulose, and hemicellulose contents, of AC have an impact on its porosity. Lignin may withstand the damaging reactions of the activation process due to its high stability and low reactivity. Since lignin is primarily responsible for developing the AC carbon skeletons and giving it its porous structure, the fixed carbon percentage in the implemented precursor is related to its lignin content (36). The contents of hemicellulose and cellulose in the source material are vital for releasing volatile matters besides their responsibility to create a meso and macro porous AC (37). The obtained ultimate, proximate, and component analysis outcomes of the BAS utilized in this work were comparable to those established by Li et al. (38).

3.2 Optimization of AC Synthesis

The impact of the IR of $ZnCl_2$ besides the activation temperature and duration, on the AC yield and IN were investigated. Selecting the proper IR of the activating agent has a practical impact on the AC features, as it affects its porous structure and enlarges the forming pores (39). The AC yield dropped with rising the activator IR from 1:1 to 3:1, as presented in **Table 1**. This outcome suggests that the activator makes the impregnated samples in evolving more volatile materials from its lingo-cellulosic structure as aldehydes, H_2O, tar, CH_4, CO, and CO_2. This removal of volatiles accounts for the carbon content of the pristine feedstock. Increasing the activator IR: feedstock will promote the evolution of more volatiles from the feed skeleton, thereby decreasing the AC yield (40). Preparation of AC samples from soybean straw (41), Fox nutshell (42), wild mustard stems (43) via $ZnCl_2$ activation displayed the same conclusions. The IN of the AC samples declined as the amount of $ZnCl_2$ increased. The best IN was obtained at 1:1 $ZnCl_2$: feed IR indicating that this ratio created an AC with a microporous structure. Above the best ratio of impregnation, the IN dropped because of the widening of micropores into mesopores besides further burn-off of the carbon (40). Hussein and Fadhil (40) and Fadhil and Kareem (44) declared similar findings upon creating AC from mixed biowastes and mixed date pits and olive stones, respectively.

The activation temperature dramatically influences the textural structures as well as the physical and chemical properties of AC. The AC yield diminished progressively as the temperature of activation raised from 400 °C to 800 °C, as displayed in Table 1, because of the extra devolatilization and dehydration of the impregnated samples (43). Demiral et al. (45) also announced comparable consequences upon transforming pumpkin seed shells into AC via the $ZnCl_2$ activation. Table 1 shows a rise in the IN from 1244.5 mg/g to 1442.33 mg/g as the temperature of activation increased from 400 °C to 500 °C. This finding is originated because of further elimination of the volatiles besides extra dehydration of the impregnated samples, leading to create an AC with a more micro-porous structure (43). Beyond 500 °C, the IN due to the possibility of the degradation of the walls of micro-pores walls in addition to the creation of meso and macro-pores at the expanse of micro-pores. $ZnCl_2$ activation of mixed date pits and olive stones (44) and pumpkin seed shell (45) for AC preparation have been observed previously.

Table 1: Effect of preparation conditions on the AC yield and IN.

$ZnCl_2$: feedstock	**Yield (wt.%)**	**IN (mg/g)**
1.0	29.57 ± 1.50	1350.55 ±2.0
2.0	25.31 ± 1.0	1235.28±1.50
3.0	23.11 ± 1.0	1127.50 ±1.50
Temperature = 600 °C; Time of activation= 90 minutes; Size of particle = 0.40 mm		
Temperature (°C)	**Yield (wt.%)**	**IN (mg/g)**
400	28.88 ± 1.50	1244.55 ±1.50
500	23.46 ± 1.50	1443.23 ±1.25
600	21.01± 2.0	1350.12 ±1.50
700	20.55 ± 1.0	1155.34 ±1.50
$ZnCl_2$:feedstock =1:1; Time of activation = 90 minutes; Size of particle = 0.40 mm		
Time (minutes)	**Yield (wt.%)**	**IN (mg/g)**
30	30.55 ± 1.25	1122.35 ± 1.50
60	23.46 ± 1.50	1443.23 ± 1.25
90	21.23± 1.50	1375.77 ± 1.25
120	20.55 ± 2.0	1188.65 ± 2.00
$ZnCl_2$:feedstock=1:1; Temperature= 500 °C; Size of particle = 0.40 mm		

It can be seen in Table 1, which offers the activation period influence on the yield and IN of the created samples. The AC yield was diminished when the activation period expanded from 30 minutes to 120 minutes due to the further dehydration of the impregnated samples, leading to a decline in the AC yield. At the same time, an enhancement in the IN was seen with extending the period of activation from 30 minutes to 60 minutes. This consequence could be ascribed to the creation of more micropores of new microporous structure. Duration above 60 minutes diminished the IN due to the distortion or expansion of the micro-pores into mesopores (43). Mohammed-Taib and Fadhil (43) and Fadhil and Kareem (44) declared the same consequences upon the $ZnCl_2$ activation of wild mustard stems and mixed date pits and olive stones for AC synthesis, respectively.

3.3 Characterization of the AC from BAS

The FESEM image of the AC synthesized from BAS via $ZnCl_2$ activation, depicted in Figure 2, exhibited that its surface contains a porous structure. The FE-SEM image demonstarted that the AC surface is rough with the occurrence of multiple pores of various sizes on it. These pores are expected to play a vital role in trapping the MO molecules as well as help in diffusing them into the porous structure of the AC. The occurrence of pores of various sizes on the AC surface will also help in the deep diffusion of the MO molecules. Besides, the FE-SEM image affirmed that BAS activation by $ZnCl_2$ at 500 °C creates many micropores, significantly enhancing the AC surface area. The formation of micropores attributes the activating agent's activity to the evolution of most organic volatiles from the original BAS structure, leaving behind a well-developed micro-porous surface.

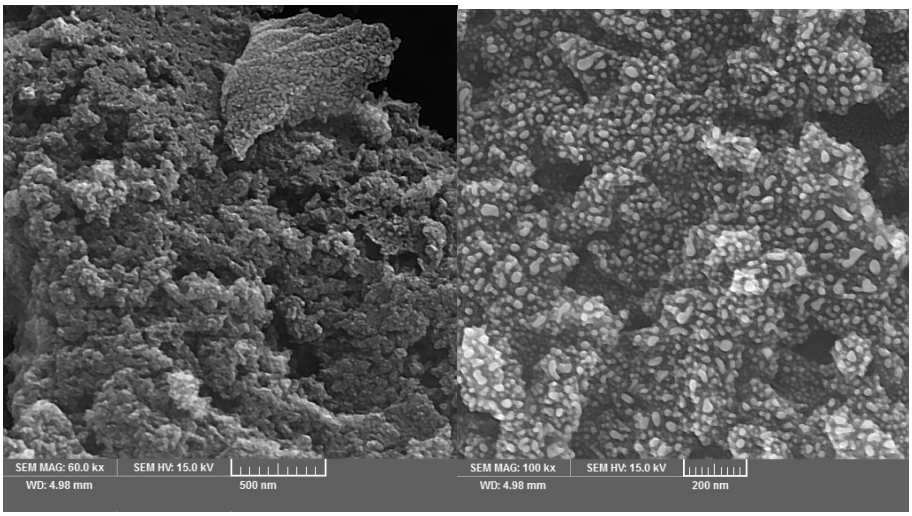

Figure 2: FE-SEM images of the typical AC sample.

The outcomes deduced from the EDS (Figure 3) disclosed an increase in the C content and a decrease in the O content after the activation process. This consequence ascribes to the pyrolytic action of the activator ($ZnCl_2$), which causes the devolatilization of the organic ingredients in the form of gaseous products and liquid tar, leaving a material with a high content of C and a low content of O (46). Additionally, Zn was observed after the activation carbonization, which is expected due to using $ZnCl_2$ in the activation process (47).

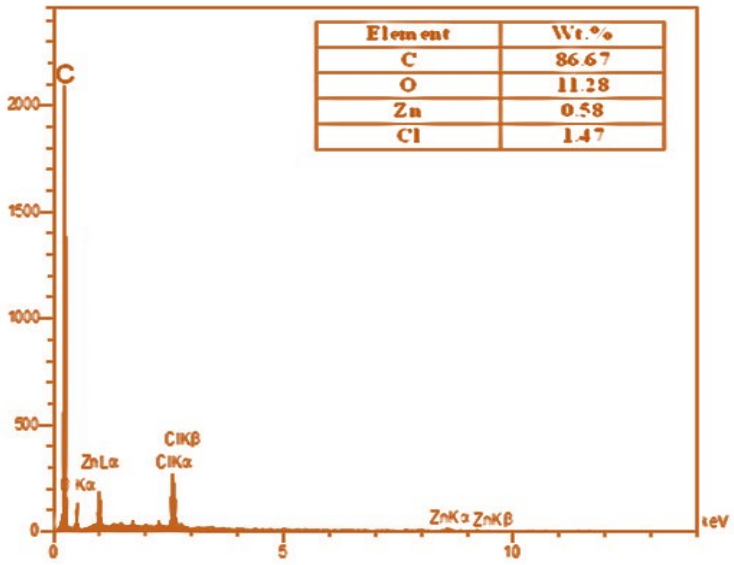

Figure 3: The EDS analysis results of the typical AC sample.

The N_2 adsorption/desorption isotherm (Figure 4) of the so-prepared AC indicates that the AC from BAS disclosed the characterization of type I adsorption isotherms. At the same time, its hysteresis belongs to IV types as per the IUPAC classification. This isotherm mainly indicated considerable development of mesoporous AC.

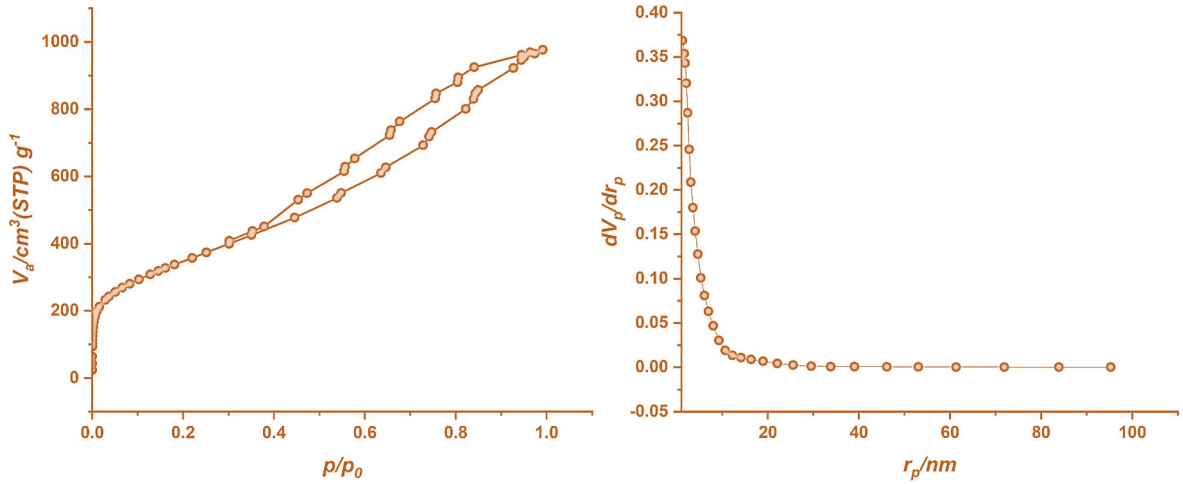

Figure 4: The N_2 adsorption/desorption isotherm and pore volume of the AC at 77 K.

At P/P_0 0.1, the adsorption showed a fast developing trend, then slowed but continued to grow clearly, confirming the possibility of the molecular monolayer adsorption phenomenon or microporous adsorption of multilayer. After P/P_0 > 0.4, a hysteresis loop was discovered, indicating that capillary condensation and inhomogeneous adsorption had occurred, demonstrating the presence of mesoporous particles (47). The so-synthesized AC possessed a SA_{BET} of 1221.60 m^2/g. A the same time, this sample showed its mesoporosity due to its average pore size, which was 2.10 nm.

The AC prepared via the $ZnCl_2$ activation of BAS exhibited a SA_{BET} greater than that established for the AC prepared through $ZnCl_2$ activation of date pits, which was 1061.3457 m^2/g(48). Table 2 lists the texture, amounts of the total acid and basic sites, and pH_{PZC} of this AC.

Table 2: Surface area, pore volume, surface functional groups amounts, and pH_{PZC} of the AC derived from BAS.

Property	AC
BET surface area (m^2/g)	1221.60
Langmuir surface area (m^2/g)	942.82
t-Plot micropore area (m^2/g)	1246.70
V_{total} ($cm^3\ g_{-1}$)	1.5091
Mean Pore Diameter width (nm)	4.98
Iodine adsorption number (mg/g)	1443.23 ±1.0
Total acid sites (mmol/g)	0.5225 ±0.001
Total basic sites (mmol/g)	0.2422 ±0.001
pH_{PZC}	4.40

Diverse functional groups could occur on the AC surface depending on the precursor implanted in its preparation and the preparation route. These groups are significant to the AC as they specify its quality as well as surface features (46).

Figure 5: The FTIR spectrum of the BAS-derived AC.

The FTIR spectrum of the AC, which is demonstrated in Figure 5, disclosed the occurrence of multiple functional groups. The Boehm titrations results showed that the chemical activation of the BAS by $ZnCl_2$ provided the surface of the attained AC with oxygenated acidic groups rather than basic groups. The value of pH_{PZC}, which was 4.40, also confirmed this conclusion. These findings were consistent with those found in the literature (40,46). The strong, broad peak around 3435 cm^{-1} belongs to the O-H stretching group of phenol, alcohol, or carboxylic acid. The bands around 2926 cm^{-1} and 2858 cm^{-1} are respectively related to asymmetric and symmetric C-H stretching vibrations (49). The absorption band observed at 1655 cm^{-1} represents the stretching carboxylate bonds. The bands from 1565 to 1471 cm^{-1} are attributed to the aromatic ring modes. The O-H bending bonds are represented by the band seen at 1384 cm^{-1} (50). Bands between 877 cm^{-1} and 750 cm^{-1} relate to the C-H aromatic out-of-plane (50). Lastly, the Zn-O stretch for the AC could be identified at 625 cm^{-1} (51).

The XRD pattern of the prepared AC is shown in Figure 6. This pattern revealed two broad phases at 2θ ranging from 20° to 30°. This pattern belongs to (002) phase, while the (100) is repserented by the broad peak in the range 40° and 50°. The occurance of these two phases in the XRD pattern assured that previously mentioned AC owns an amorphous structure (43).

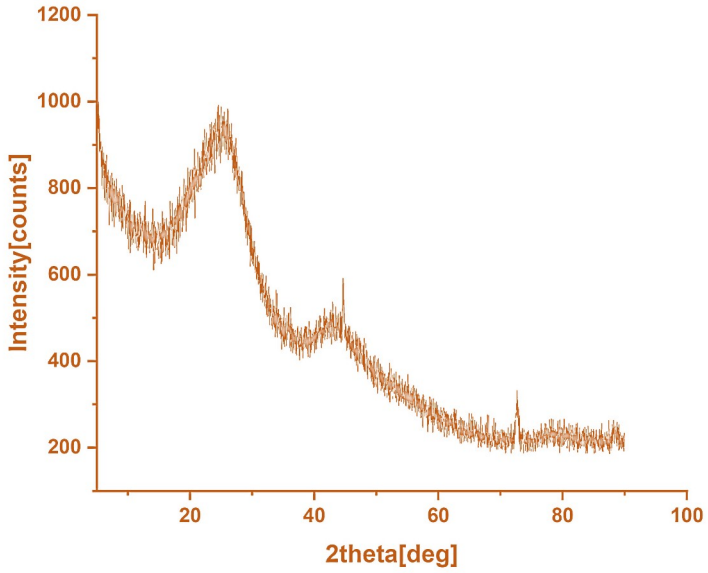

Figure 6: The XRD pattern of the BAS- derived AC.

3.4 Optimization of MO Adsorption

The influence of many variables on the adsorptive elimination (AE) of MO using BAS derived AC was investigated, as follows:

3.4.1 Influence of the initial pH

The initial pH of the working solution greatly influences the adsorption process of any pollutant. This factor affects both the functional groups existing on the AC surface besides molecular ionization of the dye, which in turn affects the interactions between both phases (24). Therefore, several adsorption experiments were accomplished between the AC and MO solutions at various values of pH (2, 3, 4, 6, 7, 8 and 10) by adding NaOH or HCl. The MO adsorption dependence on pH is presented in Figure 7, which disclosed that a pH value of 2.0 exhibited the maximum MO% removal. In contrast, the MO% removal declined with raising the solution pH over 2.0. The obtained findings assure that the acidic pH is the best for MO elimination by the as-prepared AC, which is in line with conclusions established in the literature (48,49). This outcome can be explained as follows: In an aqueous solution, MO will dissociate to give the dye ions ($R\text{-}SO3^-$) and (Na^+). In the acidic pH, the AC surface will be protonated, making its surface to be a positive charge, which in turn increases MO's adsorption by the AC due to the increment of the electrostatic interactions, namely dipole-dipole or hydrogen bonding between the AC surface (+ve) and the MO anions (-ve). In contrast, in the basic pH, the surface of the created AC will become negatively charged due to high numbers of OH^- ions on its surface, which causes the repulsion between the negatively charged surface of the AC and the dye anions, leading to lower adsorption.

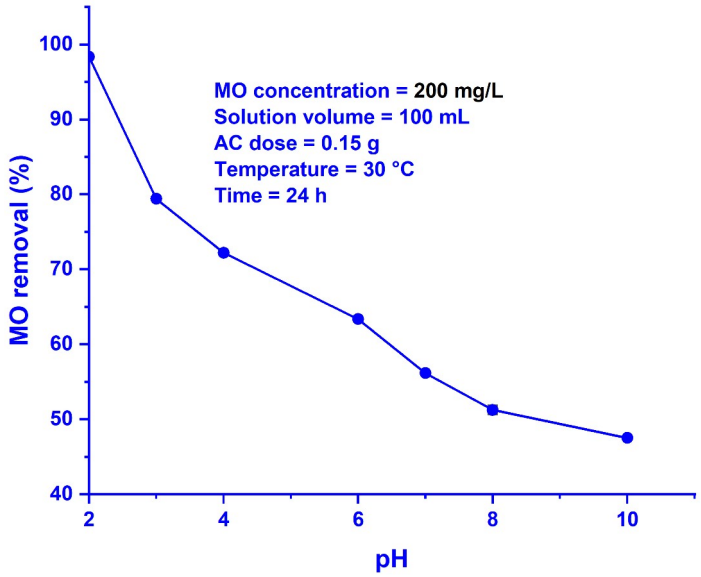

Figure 7: pH influence on MO elimination by the AC.

The pH_{PZC} of BAS-derived AC was 4.30, suggesting that the AC surface is positively charged due to the pH of the solution, which exhibited the maximum removal of MO was 2.0, which is lower than pH_{PZC} (52,53). Determining the quantity of the acidic and basic functional groups present on the AC surface was accomplished as per the Boehm titration method. The results revealed that the amount of acidic effective groups on the AC surface was nearly twice that of basic groups (Table 2), suggesting the acidic nature of the surface of the AC originated from BAS. Figure 8 illustrates the pH_{PZC} of the as-created AC.

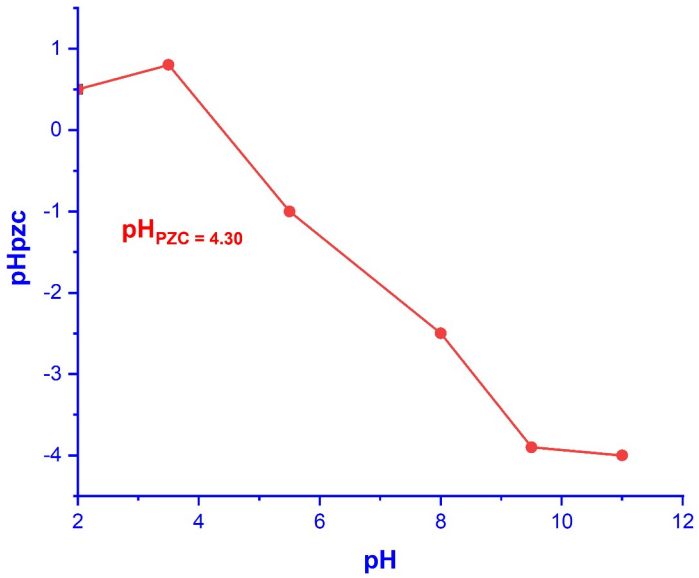

Figure 7: pH_{PZC} of the AC originated from BAS.

3.4.2 Influence of the MO initial concentration

The influence of the MO initial concentration on its adsorption capacity (q_e, mg/g) and removal efficiency (%) is given in Figure 9, which implies that by increasing the MO initial concentration from 50 mg/L to 400 mg/L, the q_e value raised from 23.0 mg/g to 194.0 mg/g due to raising the MO initial concentration increases the number of MO species per mass unit of AC, resulting in an improved interaction between the MO molecules and the AC particles.

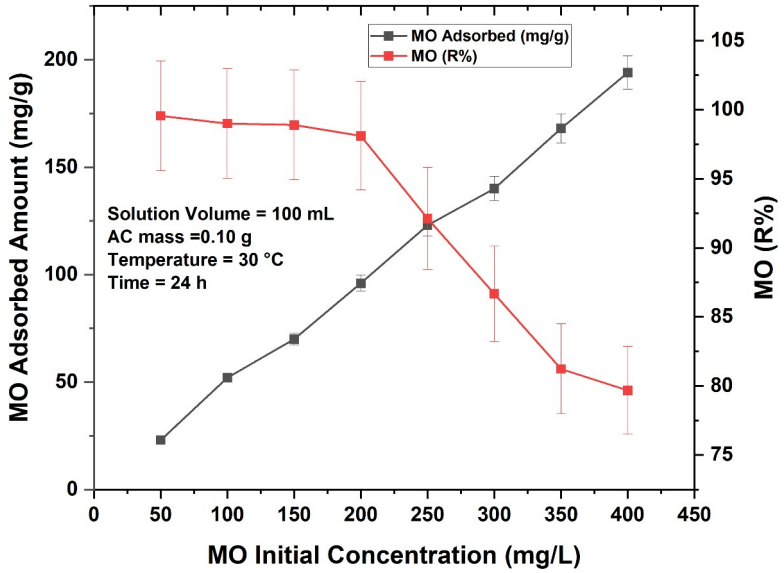

Figure 9: The initial concentration influence on the adsorptive capacity and efficiency by the AC.

In addition, increasing the sorbate initial concentration will supply the necessary driving force required to alleviate the resistance between the MO liquid phase and the AC solid phase (52). It is evident from Figure 9 that MO % removal declined with increasing the MO initial concentration. This phenomenon is explained by the fact that the number of active sites available for MO adsorption is fixed, but the number of MO molecules increases with rising MO concentration. As a result, the active sites will be rapidly depleted, resulting in a decrease in the MO R% (53).

3.4.3 Influence of the AC dosage

Because of the positive impact of AC dosage on MO R%, the effect of this parameter was investigated by attempting multiple doses of AC ranging from 0.05 g to 0.40 g.

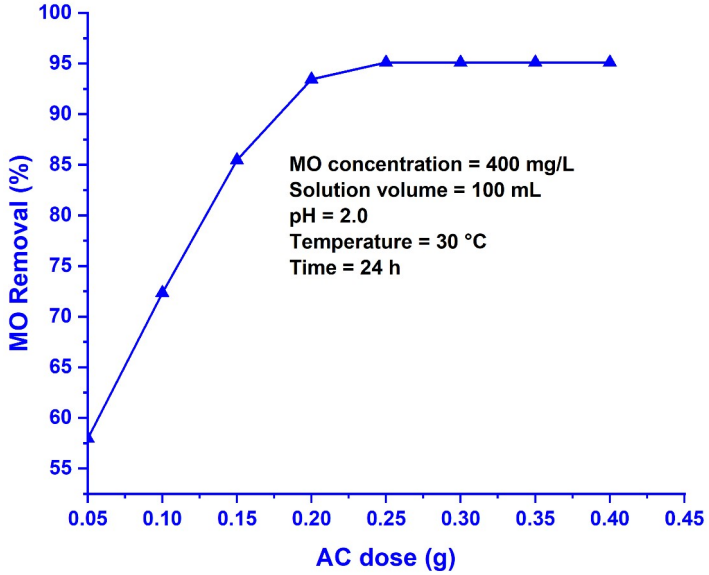

Figure 10: Influence of the AC dose on the adsorptive removal of MO.

The experiments were carried out under the conditions specified in Figure 10's legend, which implies that the MO % removal enhanced from 57.97 % to 95.11% when the AC dose increased from 0.05 g to 0.25 g. The high uptake of MO with increasing AC dose could be attributed to the fact that increasing the AC dose provides a greater number of AC particles, which means higher SA and more active sites available to adsorb the MO molecule in the solution (28). Further increasing the AC dosage had no effect on the MO R%, indicating that the equilibrium between MO-free molecules and the AC particles in the solution was attained. Other researchers have announed similar consequences(55).

3.4.4 Influence of temperature and contact time

The effect of temperature on the MO uptake of the prepared AC was investigated by conducting experiments at three different temperatures, 303, 313, and 323 K. The trials were completed using the conditions fixed in the legend for Figure 11. The MO uptake increases with rising temperature due to increasing the adsorption temperature is accompanied by a rise in the system entropy, which enhances the collisions among the AC particles and MO species. This will enhance the activity at the interface between the adsorbent and adsorbate (52). Additionally, the solution viscosity declines as the system temperature increases, leading to a better collisions among the two phases. Consequently, the MO % becomes better (53). In addition, the improvement of MO elimination with rising temperature reflects the endothermic nature of MO adsorption.

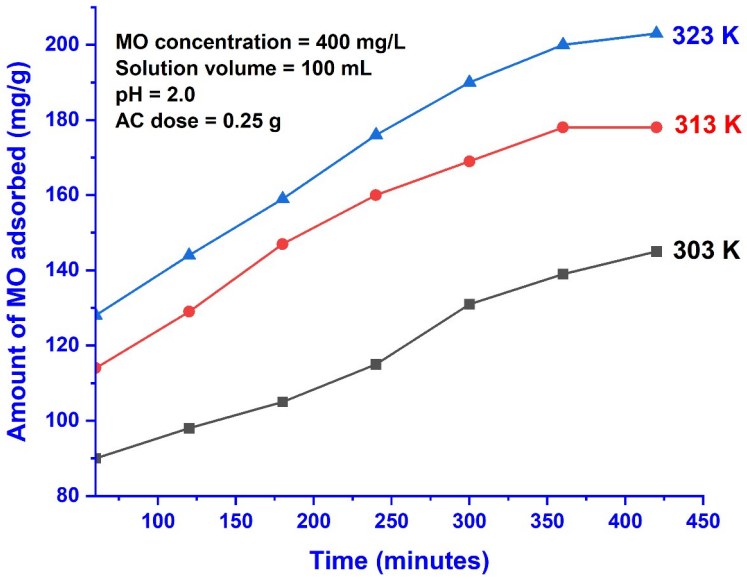

Figure 11: The impact of temperature and time on MO adsorption by the BAS-derived AC.

The contact time impact the MO elimination by the AC was inspected at various time intervals in the range of 60 –540 minutes, which is also presented in Figure 11. The adsorption experiments were done utilizing the ideal conditions obtained earlier. The consequences illustrated in Figure 11 imply that the AR of MO by BAS-derived AC enhanced when the contact period between the two phases increased. It can be seen that after 60 minutes of the process, high uptake of the MO was noticed, indicating the spontaneity of the process. This outcome attributes to the rapid adsorption in the initial steps due to the larger surface area of the adsorbent accessible to adsorb the MO molecules. The equilibrium was attained after 420 minutes. When the balance is reached, the MO molecules will occupy the most active sites, and the active positions will be unreachable. This may generate a repulsive force between the adsorbate on the adsorbent surface and in the bulk phase (49).

3.5. Adsorption Isotherms and Kinetics of MO on BAS-Derived AC

The adsorption mechanism can better be recognized by analyzing the adsorption isotherms of MO on the so-synthesized AC. As such, namely the Langmuir (Figure 12a), Freundlich (Figure 12b), and Temkin (Figure 12c) isotherms, were applied to inspect the MO adsorption data by the BAS-derived AC at multiple adsorption temperatures (303 K, 313 K, and 323 K).

From the theoretical point of view, the Langmuir model suggests monolayer adsorption onto the solid surface. It also indicates the effectiveness of the active sites toward the adsorption of the pollutant species because of the diminish of interactions among the pollutant species (24). The Langmuir constants q_m and K_L can be calculated from the plot slope and intercept, respectively, while the dimensionless separation factor (R_L) was calculated using the following equation :

$$R_L = \frac{1}{1 + C_0 K_L} \quad \text{(Eq. 10)}$$

This factor can express the favorability of adsorbate adsorption onto the adsorbent surface. Also, this factor suggests many cases of the adsorption process, e.g. the reaction is irreversible if the value of R_L = 0, while the reaction is linear if the value of R_L = 1 (40). Relating to adsorption, the latter will be favorable if 0 < R_L < 1, while the adsorption will be unfavorable when R_L > 1. The Freundlich model suggests multilayer adsorption on the solid surface. It also proposes that the solid surface is heterogeneous with the occurrence of different-affinity active sites onto the material surface (43). The the slope and the intercept of the Freundlich linear plot will provide its constants, namely *n* and K_F. The favorability of the adsorption onto the solid surface can be determined by the value of n, which suggests the adsorption favorability when its value is greater than 1.0. Because n > 1.0, the MO adsorption by the BAS-derived AC is preferable (40). The Temkin constants B and K_T can be respectively obtained from the plot's slope and intercept. As per the outcomes offered in Table 3, the Langmuir model exhibited higher R^2 values than those related to the Freundlich and Temkin models. Moreover, the q_m values for the Langmuir model were above than those observed for K_F and B, suggesting that the MO adsorption by BAS-derived AC can better be expressed by the Langmuir model than the Freundlich and Temkin models, indicating that the MO adsorption onto the surface of the obtained AC happens in monolayer so that the interactions among the MO molecules is inhibited due to the adsorption happens onto active sites with the same energy (40,44).

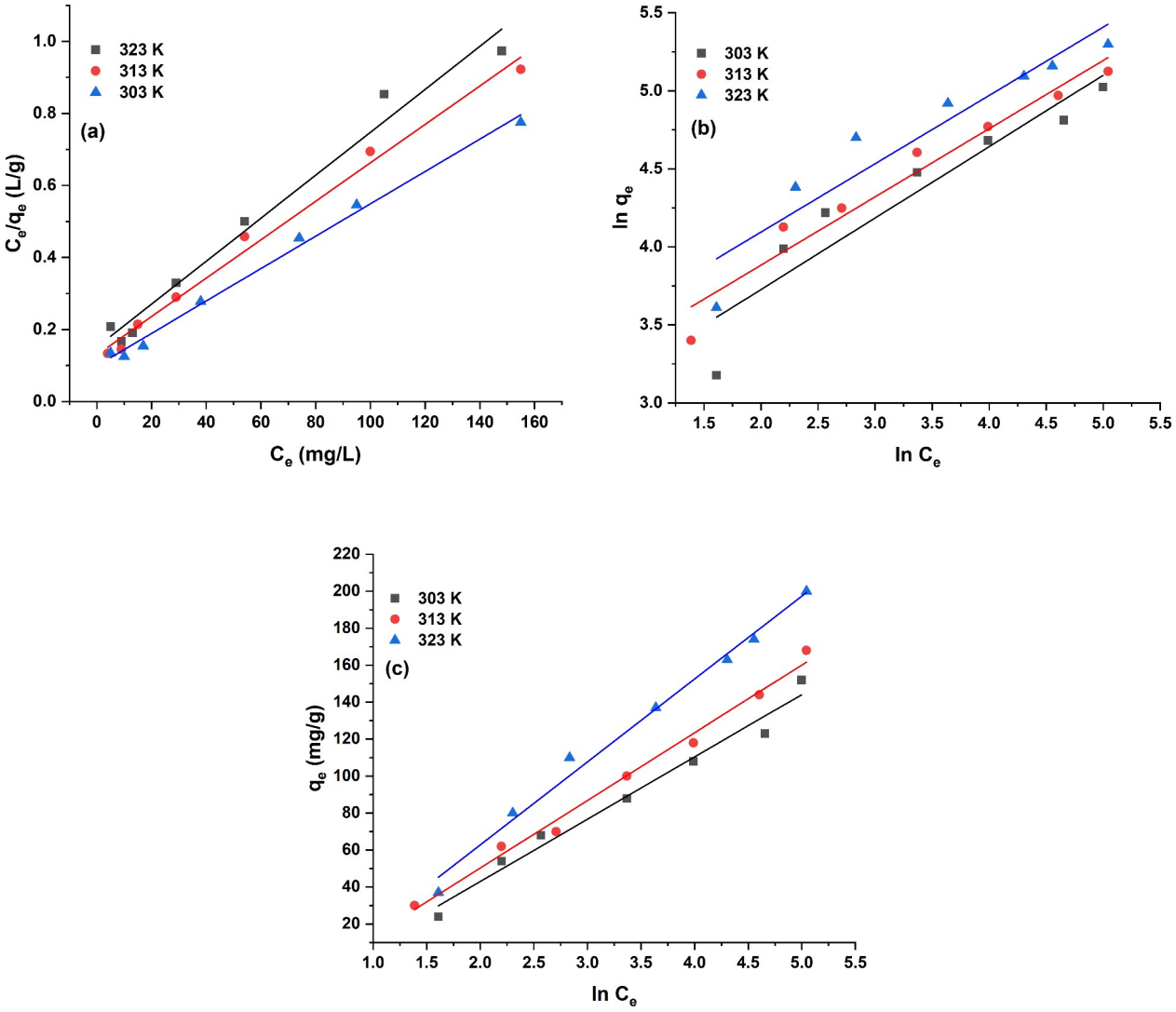

Figure 12: The adsorption isotherms of (a) Langmuir, (b) Freundlich, (c) Temkin for MO adsorption by the BAS derived AC at multiple temperatures.

Table 3: The constants of the Langmuir, Freundlich, and Temkin for the MO adsorption by the BAS derived AC.

T = 303 K									
Langmuir constants				**Freundlich constants**			**Temkin constants**		
R^2	**q_m (mg/g)**	**K_L**	**R_L**	**R^2**	**n (mg/g)**	**K_F**	**R^2**	**B (mg/g)**	**K_T (kJ/mol)**
0.9852	163.93	0.0411	0.0583	0.8825	0.45	2.82	0.8529	32.88	0.7256
T = 313 K									
Langmuir constants				**Freundlich constants**			**Temkin constants**		
R^2	**q_m (mg/g)**	**K_L**	**R_L**	**R^2**	**n (mg/g)**	**K_F**	**R^2**	**B (mg/g)**	**K_T (kJ/mol)**
0.9920	185.52	0.0421	0.0417	0.9507	0.4350	3.41	0.9919	36.26	0.6944
T = 323 K									
Langmuir constants				**Freundlich constants**			**Temkin constants**		
R^2	**q_m (mg/g)**	**K_L**	**R_L**	**R^2**	**n (mg/g)**	**K_F**	**R^2**	**B (mg/g)**	**K_T (kJ/mol)**
0.9940	224.71	0.0448	0.0528	0.8959	0.4358	3.22	0.9889	44.70	0.6655

Besides the equilibrium time, the adsorption process's efficiency can be controlled by recognizing the adsorption kinetics. The latter can also describe the adsorbate uptake rate onto the AC (33). So, three famous models, namely the pseudo-1st-order model (Figure 13a), pseudo-2nd-order model (Figure 13b), and Intra-particle diffusion model (Figure 13c) were fit to the adsorption data of MO on the BAS-derived AC so as to recognize steps controlling the MO adsorption by the said AC. The MO adsorption on the aforesaid AC was accomplished at multiple temperatures (303, 313, and 323 K). The obtained data were analyzed by applying the linear forms of those models.

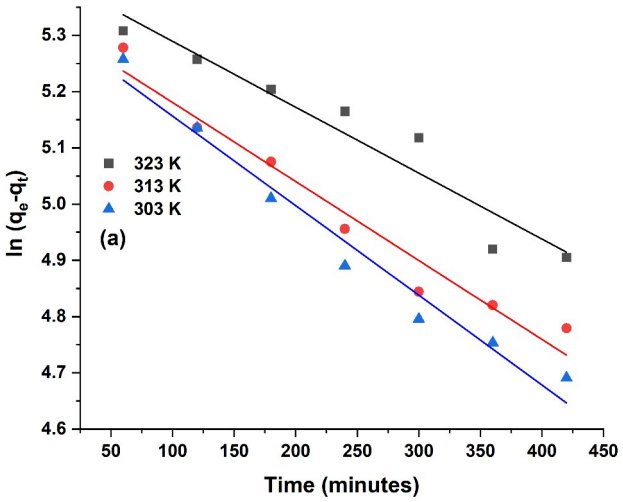

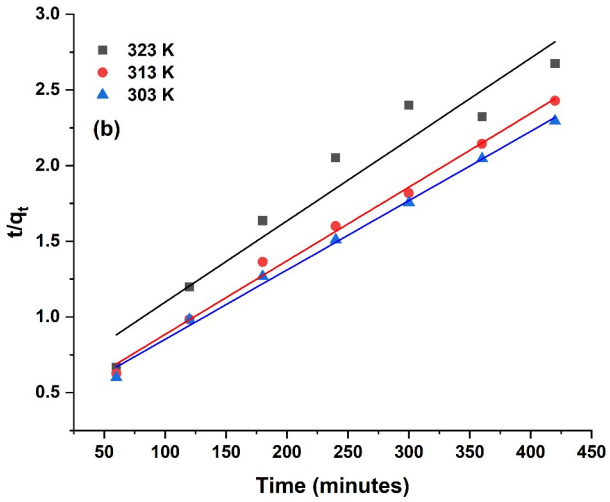

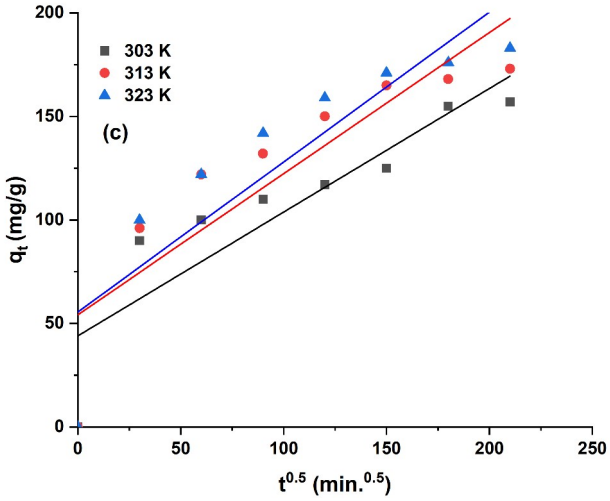

T = 313 K								
Pseudo-1st-order			**Pseudo-2nd-order**			**Intra-particle diffusion**		
R^2	**q_e (mg/g)**	**k_1**	**R^2**	**q_e (mg/g)**	**k_2**	**R^2**	**C**	**K_{id}**
0.9602	1.71	0.0020	.99438	212.76	0.00049	0.7673	54.16	0.6817
T = 323 K								
Pseudo-1st -order			**Pseudo-2nd -order**			**Intra-particle diffusion**		
R^2	**q_e (mg/g)**	**k_1**	**R^2**	**q_e (mg/g)**	**k_2**	**R^2**	**C**	**K_{id}**
0.9717	1.67	0.0015	0.9954	222.20	0.00048	0.7618	58.20	0.7178

The intra-particle diffusion model of Weber was also used to examine the MO experimental adsorption data. This model can suggest mechanisms and rate-controlling steps that affect

the kinetics of MO adsorption (57). It is clear from Figure 15, which depicts Weber's intra-particle diffusion model, that this model cannot be used solely to describe the rate-limiting step of MO adsorption by the BAS-derived AC because none of the regression plots pass through the origin, suggesting that another mechanism could have occurred (58).

3.6 Adsorption Thermodynamics

As per the adsorption outcomes, thermodynamic parameters viz. ΔH°, ΔS°, and ΔG°, were calculated. These functions, in addition to spontaneity, can provide information about the adsorption process, such as exothermicity or endothermicity, potential rise or decline in randomness at the solid/liquid interface (59). The explanation of the adsorption mechanism can be deduced from these functions as well (59). The calculation of these functions for MO adsorption by the AC originated from the BAS was accomplished at multiple temperatures, namely 303, 313, and 323 K. The following equations were utilized in the calculation of ΔH°, ΔS°, and ΔG° (51-53,59):

$$\ln\left(K_c\right)=\frac{\Delta S_o}{R}-\frac{\Delta H_o}{RT} \quad \text{(Eq. 11)}$$

$$\left(\frac{q_e}{C_e}\right)=K_c \quad \text{(Eq. 12)}$$

$$\Delta G_o=-RT\ln K \quad \text{(Eq. 13)}$$

where, K_c represents the equilibrium constant. Plotting ln K_c vs 1/T yields a straight line with a slope of ΔH° and an intercept of ΔS°, according to the van't Hoff equation. Table 5 shows the ΔH°, ΔS°, and ΔG° values, and the result reveals that the MO adsorption by the so-synthesized AC was endothermic. This conclusion was drawn from the ΔH° value, which was 9.51 kJ/mole, indicating that the MO adsorption by this AC is temperature-dependent and endothermic. This was expected because the adsorption of MO by the AC from BAS increased as the temperature rose from 303 K to 323 K. Furthermore, because of the negative values of ΔG° at different temperatures, the MO adsorption by the BAS-derived AC was spontaneous.

It was reported that when the values of ΔG° are in the range of (–20 to 0.0 kJ/mol); the adsorption is physical, while the values in the range of (– 400 to – 80 kJ/mol) suggest chemisorption (60).

The (+ve) value of ΔS° indicates an increase in the adsorption's entropy due to the adsorption and desorption phenomenon that could be involved during the solid-liquid adsorption process. This will reduce the randomness of the MO adsorption and raises it during the desorption of water molecules from the adsorbent's superficial layer (59). Similar observations were also announced by Hussain et al. (59) during the MO adsorption over chitosan composite films. The values of ΔG° for MO adsorption by the so-prepared AC were between – 2.56 to – 3.46 kJ/mol, offering that the adsorptive removal of MO by the AC surface is physical. It is accomplished through electrostatic attraction and H-bonding, as demonstrated by FTIR analysis and batch adsorption studies (60).

Table 5: Thermodynamic parameters for eliminating MO by the AC from BAS.

Temperature (K)	ΔG° (kJ/mol)	ΔH° (kJ/mol)	ΔS° (kJ/mol.K)
303	–2.56	9.51	31.42
313	–2.86	-	**-**
323	–3.46	-	**-**

3.7 Comparison of the Adsorptive Capacity

The adsorptive capacity of MO by AC prepared from BAS was compared to those of other AC samples reported in the literature, as well as other adsorbents, as tabulated in Table 6. The aforesaid created AC possessed an adsorptive capacity for MO comparable to those established for other adsorbents in the literature and, in most cases, better. The variances in the adsorptive capacity of BAS-derived AC to MO compared to the adsorbents may be ascribed to many factors, including the SA_{BET} of the adsorbent implemented besides its pore width, total pore volume, and the amount of the acidic or basic groups onto its surface. Also, the volume of the MO solution implemented, the typical pH value, and the type of mechanism involved in the adsorption process, can also affect the MO removal by any given adsorbent.

3.8 Reusability Experiments

Besides the amount of solid waste remaining, the adsorbent cost specifies the efficiency of the adsorption method used in wastewater treatment. Here, the regeneration trials of the so-prepared AC were done in an acidic medium promoting MO desorption. Outcomes from the reusability trails, which are demonstrated in Figure 14, showed a successive decline in the AR of MO by the regenerated AC. This decline is due to the loss of some active sites due to the adsorption of MO species deeply in the AC pores (67). Besides, the number of functional groups available for the adsorption procrss will be reduced as an outcome of their leaching because of the successive washing by the acid. However, the AC performance remains good even after the 5th cycle.

Table 6: The adsorptive capacity of the AC from BAS to MO compared to other adsorbents.

Adsorbent	pH	Temperature (°C)	q_{max} (mg/g)	Reference
AC from aloe vera	3.0	25.0	196.10	(61)
AC from sugarcane mills boiler residue	5.0	25.0	161.80	(62)
Biochar from hazelnut shell	-	-	181.80	(63)
Biochar from glucose	-	-	147.10	(63)
Activated biochar from pomelo peel waste	3.0	25.0	163.10	(28)
Mesoporous carbon material	2.50	20	294.10	(64)
AC from phragmites australis	-	-	217.0	(65)
Nano-adsorbent	-	-	46.0	(66)
AC from BAS	**2.0**	**50.0**	**224.21**	**This study**

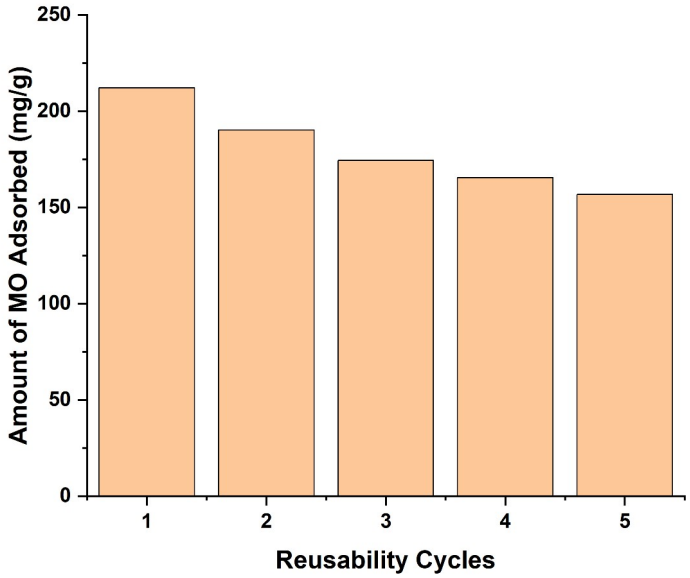

Figure 14: Reusability trails of the AC.

4. CONCLUSIONS

The BAS proved its suitability as an influential precursor in the synthesis of AC. The optimized $ZnCl_2$-activation of the BAS at an impregnation ratio of 1:1 $ZnCl_2$: BAS and 500 °C activation temperature for 60 minutes produced an AC with high SA_{BET} (1221.60 m^2/g). This AC was effective toward the adsorptive elimination of MO dye from its aqueous phase. The highest adsorptive capacity of MO by the said AC amounted to 224.71 mg/g using 0.25 g of the AC at 323 K for 420 minutes and a pH of 2.0. The Langmuir model with a maximum monolayer adsorption capacity as well as the pseudo-2nd-order kinetics best described the adsorption outcome of MO by the AC compared to other models. The thermodynamic functions of the MO adsorption by the BAS-derived AC disclosed the spontaneity and endothermic nature of MO adsorption by the said AC. Also, the adsorption of MO on the AC described above was spontaneous due to the (-ve) values of ΔG° at multiple temperatures. The mechanism of adsorption included mainly electrostatic attractions and hydrogen bonding interaction.

5. ACKNOWLEDGEMENTS

Thank is due to the Mosul University, College of Science, Chemistry Department for supporting this research work.

6. REFERENCES

1. Hasan M, Rashid MM, Hossain MM, Al Mesfer MK, Arshad M, Danish M, et al. Fabrication of polyaniline/activated carbon composite and its testing for methyl orange removal: Optimization, equilibrium, isotherm and kinetic study. Polymer Testing. 2019 Aug;77:105909. Available from: <URL>.

2. Jawad AH, Mamat NFH, Hameed BH, Ismail K. Biofilm of cross-linked Chitosan-Ethylene Glycol Diglycidyl Ether for removal of Reactive Red 120 and Methyl Orange: Adsorption and mechanism studies. Journal of Environmental Chemical Engineering. 2019 Apr;7(2):102965. Available from: <URL>.

3. Muslim M, Ali A, Neogi I, Dege N, Shahid M, Ahmad M. Facile synthesis, topological study, and adsorption properties of a novel Co (II)-based coordination polymer for adsorptive removal of methylene blue and methyl orange dyes. Polyhedron. 2021 Dec;210:115519. Available from: <URL>.

4. He W, Li N, Wang X, Hu T, Bu X. A cationic metal-organic framework based on {Zn4} cluster for rapid and selective adsorption of dyes. Chinese Chemical Letters. 2018 Jun;29(6):857–60. Available from: <URL>.

5. Bera R, Ansari M, Mondal S, Das N. Selective CO2 capture and versatile dye adsorption using a microporous polymer with triptycene and 1,2,3-triazole motifs. European Polymer Journal. 2018 Feb;99:259–67. Available from: <URL>.

6. Thamaraiselvan C, Noel M. Membrane Processes for Dye Wastewater Treatment: Recent Progress in Fouling Control. Critical Reviews in Environmental Science and Technology. 2015 May 19;45(10):1007–40. <URL>.

7. Piaskowski K, Świderska-Dąbrowska R, Zarzycki PK. Dye Removal from Water and Wastewater Using Various Physical, Chemical, and Biological Processes. Journal of AOAC INTERNATIONAL. 2018 Sep 1;101(5):1371–84. Available from: <URL>.

8. Hassan MM, Carr CM. A critical review on recent advancements of the removal of reactive dyes from dyehouse effluent by ion-exchange adsorbents. Chemosphere. 2018 Oct;209:201–19. Available from: <URL>.

9. Gadekar MR, Ahammed MM. Coagulation/flocculation process for dye removal using water treatment residuals: modelling through artificial neural networks. Desalination and Water Treatment. 2016 Nov 25;57(55):26392–400. Available from: <URL>.

10. Nourmoradi H, Zabihollahi S, Pourzamani HR. Removal of a common textile dye, navy blue (NB), from aqueous solutions by combined process of coagulation–flocculation followed by adsorption. Desalination and Water Treatment. 2016 Mar 2;57(11):5200–11. Available from: <URL>.

11. Veksha A, Pandya P, Hill JM. The removal of methyl orange from aqueous solution by biochar and activated carbon under microwave irradiation and in the presence of hydrogen peroxide. Journal of Environmental Chemical Engineering. 2015 Sep;3(3):1452–8. Available from: <URL>.

12. Mohamed EA, Selim AQ, Ahmed SA, Sellaoui L, Bonilla-Petriciolet A, Erto A, et al. H2O2-activated anthracite impregnated with chitosan as a novel composite for Cr(VI) and methyl orange adsorption in single-compound and binary systems: Modeling and mechanism interpretation. Chemical Engineering Journal. 2020 Jan;380:122445. Available from: <URL>.

13. Siyasukh A, Chimupala Y, Tonanon N. Preparation of magnetic hierarchical porous carbon spheres with graphitic features for high methyl orange adsorption capacity. Carbon. 2018 Aug;134:207–21. <URL>.

14. Kaykhaii M, Sasani M, Marghzari S. Removal of dyes from the environment by adsorption process. Chem Mater Eng. 2018;6(2):31–5.

15. Iqbal M, Saeed A, Kalim I. Characterization of Adsorptive Capacity and Investigation of Mechanism of Cu $^{2+}$, Ni $^{2+}$ and Zn $^{2+}$ Adsorption on Mango Peel Waste from Constituted Metal Solution and Genuine Electroplating Effluent. Separation Science and Technology. 2009 Oct 30;44(15):3770–91. Available from: <URL>.

16. Mekhalif T, Guediri K, Reffas A, Chebli D, Bouguettoucha A, Amrane A. Effect of acid and alkali treatments of a forest waste, *Pinus brutia* cones, on adsorption efficiency of methyl green. Journal of Dispersion Science and Technology. 2017 Apr 3;38(4):463–71. Available from: <URL>.

17. Kiwaan HA, Mohamed FSh, El-Ghamaz NA, Beshry NM, El-Bindary AA. Experimental and electrical studies of Na-X zeolite for the adsorption of different dyes. Journal of Molecular Liquids. 2021 Jun;332:115877. Available from: <URL>.

18. Aigbe UO, Ukhurebor KE, Onyancha RB, Osibote OA, Darmokoesoemo H, Kusuma HS. Fly ash-based adsorbent for adsorption of heavy metals and dyes from aqueous solution: a review. Journal of Materials Research and Technology. 2021 Sep;14:2751–74. Available from: <URL>.

19. Aichour A, Zaghouane-Boudiaf H, Djafer Khodja H. Highly removal of anionic dye from aqueous medium using a promising biochar derived from date palm petioles: Characterization, adsorption properties and reuse studies. Arabian Journal of Chemistry. 2022 Jan;15(1):103542. Available from: <URL>.

20. Hu X, Li Z, Ge Y, Liu S, Shi C. Enhanced π – π stacks of aromatic ring-rich polymer adsorbent for the rapid adsorption of organic dyes. Colloids and Surfaces A: Physicochemical and Engineering Aspects. 2022 Jun;643:128782. Available from: <URL>.

21. Xie J, Lin R, Liang Z, Zhao Z, Yang C, Cui F. Effect of cations on the enhanced adsorption of cationic dye in Fe3O4-loaded biochar and mechanism. Journal of Environmental Chemical Engineering. 2021 Aug;9(4):105744. Available from: <URL>.

22. Wang C, Yang Q, Ren N, Zhao Z, Wei W, Qin G. Preparation of loofah vine-based hierarchical porous activated carbon for methylene blue adsorption. Chemical Engineering Communications. 2022 Jan 2;209(1):62–8. Available from: <URL>.

23. Agbor Tabi G, Ngouateu Rene Blaise L, Daouda K, Naphtali Odogu A, Aime Victoire A, Nsami Julius N, et al. Non-linear modelling of the adsorption of Indigo Carmine dye from wastewater onto characterized activated carbon/volcanic ash composite. Arabian Journal of Chemistry. 2022 Jan;15(1):103515. Available from: <URL>.

24. Martini BK, Daniel TG, Corazza MZ, de Carvalho AE. Methyl orange and tartrazine yellow adsorption on activated carbon prepared from boiler residue: Kinetics, isotherms, thermodynamics studies and material characterization. Journal of Environmental Chemical Engineering. 2018 Oct;6(5):6669–79. Available from: <URL>.

25. Jiang T, Liang Y dong, He Y jun, Wang Q. Activated carbon/NiFe2O4 magnetic composite: A magnetic

adsorbent for the adsorption of methyl orange. Journal of Environmental Chemical Engineering. 2015 Sep;3(3):1740–51. Available from: <URL>.

26. Singh S, Sidhu GK, Singh H. Removal of methylene blue dye using activated carbon prepared from biowaste precursor. Indian Chemical Engineer. 2017 Dec 11;1–12. Available from: <URL>.

27. Abdullah NH, Ghani NAA, Razab MKAA, Noor AM, Halim AZA, Rasat MSM, et al. Methyl orange adsorption from aqueous solution by corn cob based activated carbon. In Kelantan, Malaysia; 2019 [cited 2023 Mar 12]. p. 020036. Available from: <URL>.

28. Zhang B, Wu Y, Cha L. Removal of methyl orange dye using activated biochar derived from pomelo peel wastes: performance, isotherm, and kinetic studies. Journal of Dispersion Science and Technology. 2020 Jan 2;41(1):125–36. Available from: <URL>.

29. Ghosh GC, Chakraborty TK, Zaman S, Nahar MN, Kabir AHME. Removal of Methyl Orange Dye from Aqueous Solution by a Low-Cost Activated Carbon Prepared from Mahagoni (Swietenia mahagoni) Bark. Pollution [Internet]. 2020 Jan [cited 2023 Mar 12];6(1). Available from: <URL>.

30. Azmi NH, Ali UFMd, Muhammad Ridwan F, Isa KM, Zulkurnai NZ, Aroua MK. Preparation of activated carbon using sea mango (*Cerbera odollam*) with microwave-assisted technique for the removal of methyl orange from textile wastewater. Desalination and Water Treatment. 2016 Dec 25;57(60):29143–52. Available from: <URL>.

31. Dai F, Muhammad Y, Gong X, Li C, Li Z, Zhang S. Low-temperature and low-pressure fuel hydrodesulfurization by solid catalyst coupling with ionic liquids. Fuel. 2014 Oct;134:74–80. Available from: <URL>.

32. Zyoud A, Nassar HNI, El-Hamouz A, Hilal HS. Solid olive waste in environmental cleanup: Enhanced nitrite ion removal by ZnCl2-activated carbon. Journal of Environmental Management. 2015 Apr;152:27–35. Available from: <URL>.

33. León G, García F, Miguel B, Bayo J. Equilibrium, kinetic and thermodynamic studies of methyl orange removal by adsorption onto granular activated carbon. Desalination and Water Treatment. 2015 Jul 25;1–14. Available from: <URL>.

34. Bilal M, Ali J, Bibi K, Khan SB, Saqib M, Saeed R, et al. Remediation of different dyes from textile effluent using activated carbon synthesized from Buxus Wallichiana. Industrial Crops and Products. 2022 Nov;187:115267. Available from: <URL>.

35. Macías-García A, Cuerda-Correa EM, Olivares-Marín M, Díaz-Paralejo A, Díaz-Díez MÁ. Development and characterization of carbon-honeycomb monoliths from kenaf natural fibers: A preliminary study. Industrial Crops and Products. 2012 Jan;35(1):105–10. Available from: <URL>.

36. Rodríguez Correa C, Stollovsky M, Hehr T, Rauscher Y, Rolli B, Kruse A. Influence of the Carbonization Process on Activated Carbon Properties from Lignin and Lignin-Rich Biomasses. ACS Sustainable Chem Eng. 2017 Sep 5;5(9):8222–33. Available from: <URL>.

37. Hong D, Zhou J, Hu C, Zhou Q, Mao J, Qin Q. Mercury removal mechanism of AC prepared by one-step activation with ZnCl2. Fuel. 2019 Jan;235:326–35. Available from: <URL>.

38. Li K, Chen H, Yu H, Zhu H, Mao Q, Ma X, et al. Study on the comprehensive utilization of bitter almond shell. BioResources. 2014;9(3):4993–5006.

39. Li Y, Li Y, Zang H, Chen L, Meng Z, Li H, et al. ZnCl $_2$ -activated carbon from soybean dregs as a high efficiency adsorbent for cationic dye removal: isotherm, kinetic, and thermodynamic studies. Environmental Technology. 2020 Jul 2;41(15):2013–23. Available from: <URL>.

40. Hussein AA, Fadhil AB. Kinetics and isothermal evaluations of adsorptive desulfurization of dibenzothiophene over mixed bio-wastes derived activated carbon. Energy Sources, Part A: Recovery, Utilization, and Environmental Effects. 2021 Mar 8;1–20. Available from: <URL>.

41. Miao Q, Tang Y, Xu J, Liu X, Xiao L, Chen Q. Activated carbon prepared from soybean straw for phenol adsorption. Journal of the Taiwan Institute of Chemical Engineers. 2013 May;44(3):458–65. Available from: <URL>.

42. Singh PK, Banerjee S, Srivastava AL, Sharma YC. Kinetic and equilibrium modeling for removal of nitrate from aqueous solutions and drinking water by a potential adsorbent, hydrous bismuth oxide. RSC Adv. 2015;5(45):35365–76. Available from: <URL>.

43. Mohammed-Taib BM, Fadhil AB. Dibenzothiophene capture from model fuel by wild mustard stems derived activated carbon: kinetics and isothermal evaluations. International Journal of Environmental Analytical Chemistry. 2021 May 26;1–23. Available from: <URL>.

44. Fadhil AB, Kareem BA. Co-pyrolysis of mixed date pits and olive stones: Identification of bio-oil and the production of activated carbon from bio-char. Journal of Analytical and Applied Pyrolysis. 2021 Sep;158:105249. Available from: <URL>.

45. Demiral İ, Aydın Şamdan C, Demiral H. Production and characterization of activated carbons from pumpkin seed shell by chemical activation with $ZnCl_2$. Desalination and Water Treatment. 2016 Feb;57(6):2446–54. Available from: <URL>.

46. Mbarki F, Selmi T, Kesraoui A, Seffen M. Low-cost activated carbon preparation from Corn stigmata fibers chemically activated using H3PO4, ZnCl2 and KOH: Study of methylene blue adsorption, stochastic isotherm and fractal kinetic. Industrial Crops and Prod ucts. 2022 Apr;178:114546. Available from: <URL>.

47. Li C, Zhang L, Xia H, Peng J, Zhang S, Cheng S, et al. Kinetics and isotherms studies for congo red adsorption on mesoporous Eupatorium adenophorum-based activated carbon via microwave-induced H3PO4 activation. Journal of Molecular Liquids. 2016 Dec;224:737–44. Available from: <URL>.

48. Cherik D, Louhab K. Preparation of microporous activated carbon from date stones by chemical activation using zinc chloride. Energy Sources, Part A: Recovery, Utilization, and Environmental Effects. 2017 Sep 17;39(18):1935–41. Available from: <URL>.

49. Georgin J, de O. Salomón YL, Franco DSP, Netto MS, Piccilli DGA, Perondi D, et al. Development of highly porous activated carbon from Jacaranda mimosifolia seed pods for remarkable removal of aqueous-phase ketoprofen. Journal of Environmental Chemical Engineering. 2021 Aug;9(4):105676. Available from: <URL>.

50. Cruz GJF, Pirilä M, Matějová L, Ainassaari K, Solis JL, Fajgar R, et al. Two Unconventional Precursors to Produce ZnCl 2 -Based Activated Carbon for Water Treatment Applications. Chem Eng Technol. 2018 Aug;41(8):1649–59. Available from: <URL>.

51. Lazarotto JS, da Boit Martinello K, Georgin J, Franco DSP, Netto MS, Piccilli DGA, et al. Preparation of activated carbon from the residues of the mushroom (Agaricus bisporus) production chain for the adsorption of the 2,4-dichlorophenoxyacetic herbicide. Journal of Environmental Chemical Engineering. 2021 Dec;9(6):106843. Available from: <URL>.

52. Yönten V, Sanyürek NK, Kivanç MR. A thermodynamic and kinetic approach to adsorption of methyl orange from aqueous solution using a low cost activated carbon prepared from Vitis vinifera L. Surfaces and Interfaces. 2020 Sep;20:100529. Available from: <URL>.

53. Mohammadi N, Khani H, Gupta VK, Amereh E, Agarwal S. Adsorption process of methyl orange dye onto mesoporous carbon material–kinetic and thermodynamic studies. Journal of Colloid and Interface Science. 2011 Oct;362(2):457–62. Available from: <URL>.

54. Zhang B, Wu Y, Cha L. Removal of methyl orange dye using activated biochar derived from pomelo peel wastes: performance, isotherm, and kinetic studies. Journal of Dispersion Science and Technology. 2020 Jan 2;41(1):125–36. Available from: <URL>.

55. Azam K, Raza R, Shezad N, Shabir M, Yang W, Ahmad N, et al. Development of recoverable magnetic mesoporous carbon adsorbent for removal of methyl blue and methyl orange from wastewater. Journal of Environmental Chemical Engineering. 2020 Oct;8(5):104220. Available from: <URL>.

56. Vali SI, Sirisha U, Poiba VR, Vangalapati M, King P. Synthesis and characterization of Titanium doped activated carbon nanoparticles and its application for the removal of dicofol. Materials Today: Proceedings. 2021;44:2290–5. Available from: <URL>.

57. Safari M, Khataee A, Darvishi Cheshmeh Soltani R, Rezaee R. Ultrasonically facilitated adsorption of an azo dye onto nanostructures obtained from cellulosic wastes of broom and cooler straw. Journal of Colloid and Interface Science. 2018 Jul;522:228–41. Available from: <URL>.

58. Dong Z, Du J, Wang A, Yang X, Zhao L. Removal of methyl orange and acid fuschin from aqueous solution by guanidinium functionalized cellulose prepared by radiation grafting. Radiation Physics and Chemistry. 2022 Sep;198:110290. Available from: <URL>.

59. Hussain S, Kamran M, Khan SA, Shaheen K, Shah Z, Suo H, et al. Adsorption, kinetics and thermodynamics studies of methyl orange dye sequestration through chitosan composites films. International Journal of Biological Macromolecules. 2021 Jan;168:383–94. Available from: <URL>.

60. Dutta SK, Amin MK, Ahmed J, Elias Md, Mahiuddin Md. Removal of toxic methyl orange by a cost-free and eco-friendly adsorbent: Mechanism, phytotoxicity, thermodynamics, and kinetics. South African Journal of Chemical Engineering. 2022 Apr;40:195–208. Available from: <URL>.

61. Khaniabadi YO, Heydari R, Nourmoradi H, Basiri H, Basiri H. Low-cost sorbent for the removal of aniline and methyl orange from liquid-phase: Aloe Vera leaves wastes. Journal of the Taiwan Institute of Chemical Engineers. 2016 Nov;68:90–8. Available from: <URL>.

62. Martini BK, Daniel TG, Corazza MZ, de Carvalho AE. Methyl orange and tartrazine yellow adsorption on activated carbon prepared from boiler residue: Kinetics, isotherms, thermodynamics studies and material characterization. Journal of Environmental Chemical Engineering. 2018 Oct;6(5):6669–79. Available from: <URL>.

63. Çağlar E, Donar YO, Sinağ A, BiRoğlu İ, BiLge S, Aydincak K, et al. Adsorption of anionic and cationic dyes on biochars, produced by hydrothermal carbonization of waste biomass: effect of surface functionalization and ionic strength. Turk J Chem. 2018;42:86–99. Available from: <URL>.

64. Mohammadi N, Khani H, Gupta VK, Amereh E, Agarwal S. Adsorption process of methyl orange dye onto mesoporous carbon material–kinetic and thermodynamic studies. Journal of Colloid and Interface Science. 2011 Oct;362(2):457–62. Available from: <URL>.

65. Chen S, Zhang J, Zhang C, Yue Q, Li Y, Li C. Equilibrium and kinetic studies of methyl orange and methyl violet adsorption on activated carbon derived from Phragmites australis. Desalination. 2010 Mar;252(1–3):149–56. Available from: <URL>.

66. Baig U, Uddin MK, Gondal MA. Removal of hazardous azo dye from water using synthetic nano adsorbent: Facile synthesis, characterization, adsorption, regeneration and design of experiments. Colloids and Surfaces A: Physicochemical and Engineering Aspects. 2020 Jan;584:124031. Available from: <URL>.

67. Fadhil AB, Saeed HN, Saeed LI. Polyethylene terephthalate waste-derived activated carbon for adsorptive desulfurization of dibenzothiophene from model gasoline: Kinetics and isotherms evaluation. Asia-Pac J Chem Eng [Internet]. 2021 Mar [cited 2023 Mar 12];16(2). Available from: <URL>.